




Significantly improved magnetic parameters of Co–La co-doped strontium hexagonal ferrites for recording applications: structural, hysteresis, and mössbauer performance metrics

Manisha Thakur¹, Charanjeet Singh^{2,*} , Kirill D. Martinson³, Ivan V. Buryanenko⁴, Valentin G. Semenov⁵, Sanjay R. Mishra⁶, Md Farhan Azim⁶, A. K. Srivastava^{1,*}, and Vadim I. Popkov³

¹ Department of Physics, School of Chemical Engineering and Physical Sciences, Lovely Professional University, Phagwara, Punjab 144411, India

² School of Electronics and Electrical Engineering, Lovely Professional University, Phagwara, Punjab 144411, India

³ Ioffe Institute, Saint Petersburg, Russia 194021

⁴ RITVERC JSC, Saint Petersburg, Russia 194223

⁵ Institute of Chemistry, Saint Petersburg State University, Saint Petersburg, Russia 198504

⁶ Department of Physics and Materials Science, The University of Memphis, Memphis, TN 38152, USA

Received: 11 July 2023

Accepted: 11 September 2023

Published online:
19 October 2023

© The Author(s), under exclusive licence to Springer Science+Business Media, LLC, part of Springer Nature, 2023

ABSTRACT

M-type hexaferrite substituted with cobalt and lanthanum [SrCo_{1.5z}La_{0.5z}Fe_{12-2z}O₁₉ (SCLF; 0.0 ≤ z ≤ 0.5)] was synthesized by auto-combustion Sol–gel methodology. XRD study indicated that prepared specimens exhibit a hexagonal magnetoplumbite phase without any secondary peak. The crystallite size decreases from 48.94 to 28.82 nm as the level of substitution increases in SrM hexaferrite. The micrographs showed an enhancement in the inter-grain connectivity of grains with substitution. Mössbauer spectra revealed the variation observed in hyperfine interactions, isomer shift, quadrupole splitting, and relative area of five sextets of Fe³⁺ ions. Analysis of Mössbauer depicted that the substituents tend to occupy spin-up 12k-2a sites of crystal lattice from z = 0.0 to z = 0.3, which elucidated the diminution observed in magnetization. The coercivity gradually decreased from z = 0.0 (5026.54 Oe) to z = 0.5 (862.47 Oe). The saturation magnetization initially decreased with substitution from z = 0.0 to 0.3 and then increased for z = 0.4 and 0.5 samples. The magnetic susceptibility (dM/dH) of samples derived from magnetic parameters is high for z = 0.0, 0.2, 0.3, and 0.4. Both M_s with tunable H_c and magnetic susceptibility results make them considerable materials for recording applications.

Address correspondence to E-mail: rcharanjeet@gmail.com; srivastava_phy@yahoo.co.in

1 Introduction

The M-type hexagonal ferrites have gained the interest of researchers and material scientists due to their unique characteristics such as low eddy current losses, chemical stability, low cost [1], mechanical rigidity, high values of curie temperature, coercivity, saturation magnetization, and uniaxial anisotropy. These properties make them preferable materials for several applications such as microwave devices [2], sensors, radiation shielding [3], memory storage devices, magneto-optical, and perpendicular magnetic recording media [4]. These hexagonal ferrites consist of a magnetoplumbite structure with the general formula $A\text{Fe}_{12}\text{O}_{19}$ (where $A = \text{Sr, Ba, Ca and Pb}$) and belongs to the space group $P6_3/mmc$. The unit cell of magnetoplumbite structure is described as RSR^*S^* , where S represents a spinel block consisting of two layers of oxygen ions ($\text{O}_4\text{-O}_4$) linked to a block R composed of three layers of oxygen ions ($\text{O}_4\text{-AO-O}_4$), where A maybe Ba^{2+} , Pb^{2+} and Sr^{2+} , etc. [5]. The blocks S^* and R^* are corresponding blocks of S and R with a 180° rotation around the c -axis, respectively. In M-type hexaferrite, 24 Fe^{3+} ions are unevenly distributed over five distinct crystallographic sites: one tetrahedral site ($4f_1$), one trigonal bipyramidal ($2b$) site, and three octahedral sites ($12k$, $2a$, and $4f_2$). Substituting these Fe^{3+} ions with a variety of cations can improve the magnetic properties of M-type ferrite. Several methods are available for synthesizing hexagonal ferrites, including the ceramic method [6], chemical co-precipitation [7], solid-state reaction [8], auto-combustion sol-gel method [9], micro-emulsion method [10]. Presently, the auto-combustion sol-gel method is preferably utilized for synthesizing hexaferrite with desirable properties such as good homogeneity, better control of particle size distribution, nanosized particle and low cost [11, 12]. To tailor hexaferrite materials for use in recording media applications and to achieve efficient and reliable data storage devices, it is necessary to delve into the various aspects of magnetization and coercivity. This investigation aims to ascertain that the magnetization and coercivity of ferrite material must be high enough to ensure that the recorded signal is stable, readable, and accurate.

Several investigations have been conducted to improve the magnetic characteristics of M-type hexaferrite through cationic substitutions. Sriramulu et al. [13] synthesized Cr-Al co-doped $\text{SrCr}_x\text{Al}_x\text{Fe}_{(12-2x)}\text{O}_{19}$ ($0.0 \leq x \leq 1.0$) hexaferrite using a

microwave-hydrothermal methodology. The results indicated a decrease in the average grain size and a change in grain shape to spherical from hexagonal with increasing the content of doping. The doping decreased M_s from 59.0 to 47.44 emu/g, and coercive force ranged from 2147 to 2715 Oe. Du et al. [14] explored the magnetic and structural properties of ceramic process synthesized Zn-substituted $\text{Sr}_{0.1}\text{La}_{0.45}\text{Ca}_{0.45}\text{Fe}_{11.7-x}\text{Zn}_x\text{Co}_{0.3}\text{O}_{19}$ hexaferrite. The intrinsic coercivity of prepared ferrites decreased continuously, while the remanence value initially increased and then decreased. Xing Suo et al. [15] enquired about the effect of La^{3+} ion on the magnetic and structural characteristics of $\text{Sr}_{1-x}\text{La}_x\text{Fe}_{12}\text{O}_{19}$ ($0.0 \leq x \leq 0.15$) hexagonal ferrites. This research involved the synthesis of La-doped M-type Sr hexagonal ferrites through the traditional solid-phase sintering process. The obtained results revealed that the obtained samples possessed a plate-like hexagonal grain structure with refined grain size as the La content increased. The magnetic properties and coercive force were found to be improved, while saturation magnetization was low (0.547 emu/g) at 702.2 Oe. Nandotaria et al. [16] comprehensively analyzed the effect of Mg^{2+} ion on Sr-Cu M-type hexaferrite nanoparticles and the saturation magnetization values raised from $x = 0.0$ (43.30 emu/g) to $x = 0.1$ (47.15 emu/g) and after that, it suddenly reduced to $x = 0.5$ (1.66 emu/g). Almessiere et al. [17] investigated magnetic susceptibility and Mössbauer spectra of Mn-Y-doped Sr hexaferrite. The researchers used the citrate sol-gel method to prepare $\text{Sr}_{1-x}\text{Mn}_x\text{Fe}_{12-x}\text{Y}_x\text{O}_{19}$ hexaferrite, where x ranged from 0.0 to 0.5. The results of Mössbauer spectra revealed that the Mn-Y ions could selectively occupy the $4f_2$, $2b$, and $12k$ sites. Rai et al. [18] studied the impact of La and Al ions on the structural and magnetic properties of $\text{SrFe}_{12}\text{O}_{19}$ hexaferrite. The result revealed a notable 73% increase in intrinsic coercivity when introducing Al^{3+} ions into $\text{SrFe}_{12}\text{O}_{19}$ hexaferrite. Furthermore, the addition of rare earth resulted in an additional 50% boost in coercivity. Chauhan et al. [19] investigated the effect of calcination temperature on magnetic and structural characteristics of La-Co substituted $\text{SrFe}_{12}\text{O}_{19}$ hexaferrite. A VSM analysis revealed the enhancement in saturation magnetization from 20.45 to 58.10 emu/g by increasing La content. Furthermore, the effect of La ions on $\text{SrFe}_{12}\text{O}_{19}$ hexaferrite has been studied for enhancing the magnetic properties by Hessian et al. [20]. The inclusion of La^{3+} ions led to a significant increase in coercivity from 275 to 2366

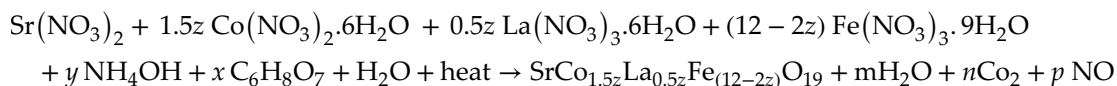
Oe. Rambabu et al. [21] comprehensively analyzed the effect of La^{3+} and Ni^{2+} ions on the structural, magnetic, and dielectric characteristics of $\text{SrFe}_{12}\text{O}_{19}$ hexaferrite. The saturation magnetization was lying in the range of 49.06 to 64.14 emu/g, while coercivity ranged from 3602 to 4642 Oe.

It has been observed from the above reports that the substitution of transition metal or rare earth ions can bring significant changes in the morphology and magnetic properties of substituted $\text{SrFe}_{12}\text{O}_{19}$ hexaferrites. It is very well known that the rare earth ions have their 4f shell shielded by $5s^25p^6$, which are not strongly influenced by the potential field created by nearby ions [22, 23]. The magnetic behavior of M-type hexaferrite is primarily governed by the configuration of 12k sites of the crystal lattice. When these sites are replaced with weak magnetic or diamagnetic ions, it disrupts the octahedral-tetrahedral super-exchange interactions. It has been reported that rare earth ions tend to occupy these lattice sites, leading to alterations in the material's magnetic characteristics. Additionally, rare earth cations with their large 4f electron shell, and cobalt, with their high magnetic moment, can contribute to improving the magnetic properties of the material. Moreover, the good crystalline nature and magnetic stable state can be determined through magnetic susceptibility plots, which have not been explored in the mentioned reports.

In the present manuscript, we have successfully synthesized the $\text{SrCo}_{1.5z}\text{La}_{0.5z}\text{Fe}_{12-2z}\text{O}_{19}$ (SCLF; $0.0 \leq z \leq 0.5$) hexaferrite by sol-gel auto-combustion methodology and study their influence through structural, morphological, Mössbauer, and magnetic characteristics.

2 Experimental procedure

The Equation of combustion reaction can be written as:



The synthesis of SCLF hexaferrite was accomplished using the auto-combustion sol-gel method. Analytical grade starting materials, including like $\text{Sr}(\text{NO}_3)_2$, $\text{La}(\text{NO}_3)_3 \cdot 6\text{H}_2\text{O}$, $\text{Co}(\text{NO}_3)_2 \cdot 6\text{H}_2\text{O}$, and $\text{Fe}(\text{NO}_3)_3 \cdot 9\text{H}_2\text{O}$, were dissolved in 100 ml of distilled water in the appropriate stoichiometric proportions. This aqueous solution

Table 1 Assignment of sample name for a different level of substitution of $\text{SrCo}_{1.5z}\text{La}_{0.5z}\text{Fe}_{12-2z}\text{O}_{19}$ hexaferrite

$\text{SrCo}_{1.5z}\text{La}_{0.5z}\text{Fe}_{12-2z}\text{O}_{19}$	Sample name
Z=0.0	SCLF 1
Z=0.1	SCLF 2
Z=0.2	SCLF 3
Z=0.3	SCLF 4
Z=0.4	SCLF 5
Z=0.5	SCLF 6

served as the precursor, by mixing all nitrates and citric acid ($\text{C}_6\text{H}_8\text{O}_7$) in a 1:1.5 ratio with the help of a magnetic stirrer. Ammonia solution was slowly added to maintain the pH of an aqueous solution of about 7. The mixture was then heated at 70–80 °C with constant stirring to avoid precipitation and make a homogeneous solution. After constant heating and stirring for about 4–5 h, the solution became gel which gets burnt off and formed a brownish powder. The prepared powder was pre-heated at 550 °C for 2 h before being calcined at 1100 °C/5 h with a rate of heating 12 °C/min. Table 1 assigns the sample name for a different level of substitution.

3 Characterization technique

For structural characterization of SCLF samples, XRD patterns under the different levels of substitution were investigated using a source of Cu-K α radiation ($\lambda = 1.5406 \text{ \AA}$) on a D8 Bruker Advance X-ray diffractometer. The infrared spectra were obtained in the transmittance mode of range 400–3000 cm^{-1} on a pellet accessory (Perkin Elmer Spectrum) and FTIR (diamond ATR). The micrographs and elemental composition of the samples were determined by SEM (scanning electron microscopy) and EDAX (energy-dispersive spec-

trospectroscopy) using a scanning electron microscope *Tescan Vega 3 SBH* and an attachment *Oxford INCA 2000*. The spectra were collected over several areas in the range up to 10 keV with the number of chI collected in the spectral channels equal to 2048 and the number of pulses per spectrum at least 1,000,000. The magnetic parameters

of hexagonal ferrites powders viz-a-viz remanent magnetization (M_r), coercive force (H_c), and saturation magnetization (M_s) were determined using a *Lake Shore 7410* vibrating magnetometer in the range of applied external field from 0 to 5000 E. The processing of the obtained hysteresis loops was carried out in the software systems "Measure Link-MCS" and "Curve Handler".

4 Results and discussion

4.1 Phase identification and lattice parameter

Figure 1 illustrates the XRD pattern of the prepared SCLF hexaferrite samples, demonstrating the reflection planes within the 2θ range of 20° – 70° agreed with the ICDD-801197 reference of M-type hexaferrite. This confirms the successful formation of single-phase M-type $\text{SrFe}_{12}\text{O}_{19}$ (SrM) hexaferrite. Figure 2 shows the enlarged view of the slight shift occurring in the high-intensity peak (107) of a prepared specimen with Co^{2+} – La^{3+} substitution. The high-intensity peak (107) displays a subtle shift of 2θ towards the right side of the Bragg angle. The observed changes in peak intensity and lattice sizes, from SCLF 1 to SCLF 6, indicate the successful substitution of Co^{2+} – La^{3+} ions at distinct crystallographic sites [24]. Table 2 lists lattice parameters (c , a , and c/a) and unit cell volume (V) estimated using Eqs. (1) and (2), and their variation with different levels of substitution is shown in Fig. 4 [25].

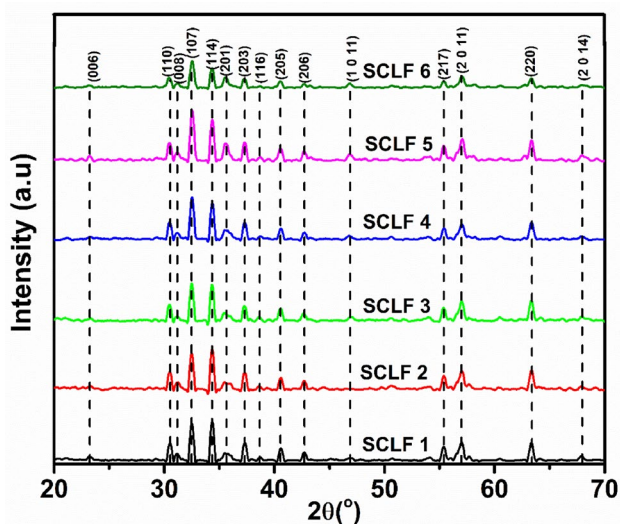


Fig. 1 XRD pattern of prepared specimen SCLF 1 to SCLF 6 hexaferrite

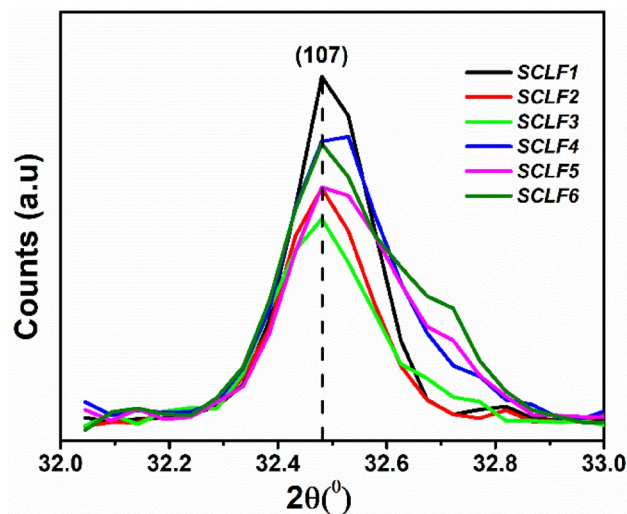


Fig. 2 An enlarged view of high-intensity peaks (107)

$$\frac{1}{d_{hkl}^2} = \frac{4}{3} \left(\frac{h^2 + hk + k^2}{a^2} \right) + \frac{l^2}{c^2} \quad (1)$$

$$V = \frac{\sqrt{3}}{2} a^2 c \quad (2)$$

where $d_{(hkl)}$ display interplanar distance which has been calculated from the relation $2d_{hkl}\text{Sin}\theta = n\lambda$ and (hkl) imply Miller indices. Table 2 presents the observed value of the lattice constant ' c ' ranges from 22.9518 to 22.9048 Å, ' a ' varies from 5.8545 to 5.8644 Å, and the unit cell volume ranges from 681.26 to 679.86 Å³. These findings (Fig. 3) indicate that the expansion of the lattice parameter ' a ' is smaller than that of the parameter ' c ' and is consistent with the conventional behavior of M-type hexaferrites [26]. The change observed in the lattice parameter is due to larger ionic radii of Co^{2+} (0.72 Å) and La^{3+} (1.15 Å) ions as compared to the host ion Fe^{3+} (0.645 Å). For the M-phase, the height-to-width ratio (c/a) should be around 3.98 and the observed values lie in the range of 3.92 to 3.91, which is close to the predicted values [27].

4.2 Crystallite size and density measurement

We can calculate the crystallite size (D) using the Debye Scherrer formula, and the specific surface area (S) using the following equations [25]:

$$D = k\lambda / \beta \cos \theta \quad (3)$$

Table 2 Diffraction angle (2θ), FWHM, Lattice constant c , lattice constant a , volume of the unit cell (V), c/a , the crystallite size, lattice strain (ϵ) for different levels of substitution SCLF 1 to SCLF 6

Sample name	2θ ($^\circ$)	FWHM	c (\AA)	a (\AA)	V (\AA^3)	c/a	Crystallite size (nm)	ϵ
SCLF 1	32.4806	0.169	22.9518	5.8545	681.26	3.92	49	0.0514
SCLF 2	32.4806	0.186	22.9518	5.8545	681.26	3.92	44	0.0210
SCLF 3	32.4806	0.209	22.9518	5.8545	681.26	3.92	39	0.0420
SCLF 4	32.5290	0.218	22.9048	5.8545	679.86	3.91	38	0.0300
SCLF 5	32.4806	0.254	22.9518	5.8545	681.26	3.92	32	0.0500
SCLF 6	32.4806	0.287	22.9357	5.8644	683.08	3.91	29	0.0070

$$S = \frac{6000}{D\rho_x} \tag{4}$$

where β is displayed as the full width at half maxima (in radians), θ implies Bragg’s angle expressed in radians, $k = 0.9$ denoted as Scherrer constant, ρ_x is the X-ray density, and λ (1.540 \AA) X-ray wavelength. The calculated values of FWHM and crystallite size are listed in Table 2. From SCLF 1 to SCLF 6, the FWHM value of the high-intensity peak becomes broader and consequently declines the crystallite size. The average crystallite size of a high-intensity peak decreases from 48.94 nm (SCLF1) to 28.82 nm (SCLF6) with the increase in the level of substitution [28, 29]. The William–Hall equation $\beta \cos \theta = k\lambda/D + 4\epsilon \sin \theta$ is used to determine the degree of deformation in the crystal lattice [30]. Its measurement is based on the lattice parameters of the crystals and their changes concerning the applied stress or strain. Figure 4 shows a plot with $\beta \cos \theta$ along the y-axis and $4\sin \theta$ along the x-axis. The average lattice strain of all prepared specimens lies between SCFF1 (0.0514)—SCLF6 (0.0070). The surface area (S) of a prepared specimen is inversely linked to the crystallite size (Eq. 4), and the value of the surface area (Table 3) gradually increases from SCLF1 to SCLF6 ($23.37\text{--}29.88 \times 10^7 \text{ cm}^2/\text{g}$).

The bulk density (ρ_{bulk}) can be calculated with the help of a pellet having thickness (h), radius (r), and mass of pellet (m) using the following expression:

$$\rho_{\text{bulk}} = \frac{m}{\pi r^2 h} \tag{5}$$

The XRD density (ρ_x) and porosity (P) of the prepared specimen can be estimated using the below expression:

$$\rho_x = \frac{zM}{N_A V} \tag{6}$$

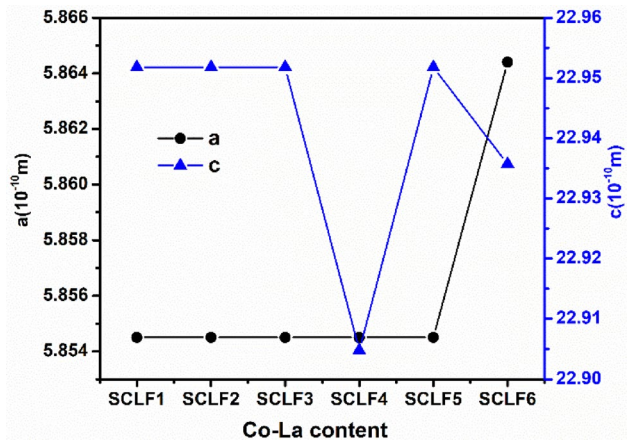
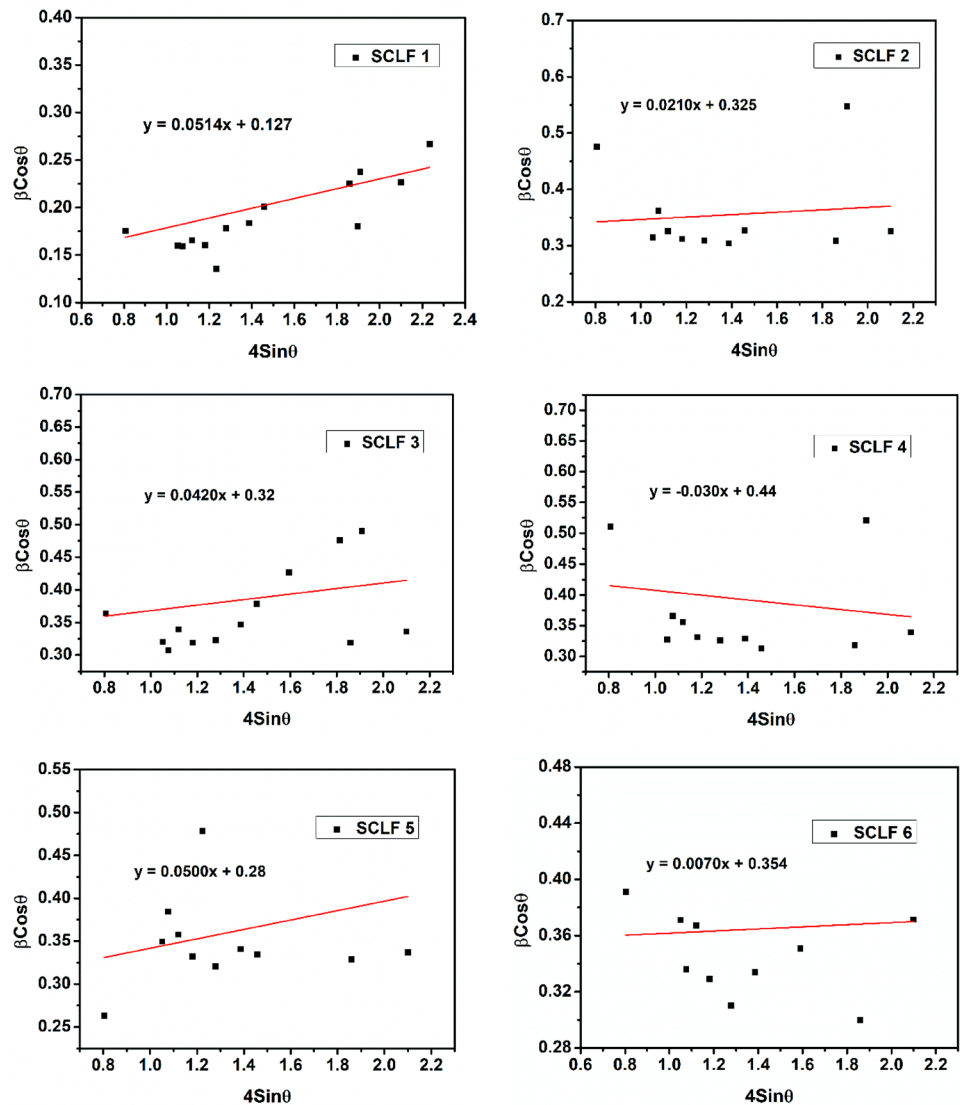


Fig. 3 Lattice constant ‘a’ and ‘c’ variation with different levels of substitution

$$P\% = \left(1 - \frac{\rho_{\text{bulk}}}{\rho_x} \right) \tag{7}$$

where N_A represent as Avogadro’s number, M implies molecular weight, z , and V imply the number of molecules per unit cell, and volume of the unit cell respectively. Substitution causes an increment in XRD density (ρ_x) from SCLF1 (5.17 g/cm^3) to SCLF6 (5.28 g/cm^3), which may be due to the lesser atomic mass of host Fe^{3+} (55.84 amu) ion than substituted Co^{2+} (58.93 amu) and La^{3+} (138.90 amu) ions, as presented in Table 3 [27]. Moreover, the value of ρ_x surpasses ρ_{bulk} , suggesting the existence of pores during the sample preparation and attributed to irregular grain shape [31]. The porosity (P) shows an irregular trend with substitution and is minimal for the SCLF1 sample (Fig. 5).

Fig. 4 William Hall plots of SCLF 1 to SCLF 6 hexaferrite



4.3 Infrared region analysis

FTIR spectroscopy serves as a valuable tool for obtaining both quantitative and qualitative insights into molecular band position, existing chemical bonds, and attached functional groups. It aids in determining the structural changes resulting from the substitution of Co^{2+} – La^{3+} ions in SrM hexaferrites [5]. FTIR spectra of the prepared specimen were examined in the infrared range from 3000 to 400 cm^{-1} , as seen in Fig. 6. Table 4 explains the position of absorption bands obtained in the IR range of 600 to 400 cm^{-1} for a different level of substitution. There are no broad absorption bands near 1385 cm^{-1} , 2750 cm^{-1} , and 3000 cm^{-1} , indicating the nonexistence of NO_3^- , C–H bending vibration, and vibrations due to the hydroxyl group (O–H),

respectively [32]. The characteristic absorption bands observed in the range of 400 – 800 cm^{-1} are mainly due to iron oxide, but instead, a new set of resolved absorption bands has been obtained [33]. The observed bands lie in the range of 500 – 600 cm^{-1} representing mode ν'' and are owed to stretching vibrations of Fe^{3+} – O^{2-} at tetrahedral sites. Other absorption bands from 400 to 450 cm^{-1} represent mode ν' and are due to vibrations of Fe^{3+} – O^{2-} at octahedral crystallographic sites of crystal structure [34]. Furthermore, the substitution of Co^{2+} and La^{3+} ions alter the band position of tetrahedral and octahedral sites towards a higher frequency side. This may confirm the successful substitution of Co^{2+} – La^{3+} ions in crystallographic sites of hexagonal crystal structure [35].

Table 3 XRD density (ρ_x), bulk density (ρ_{bulk}), porosity in % (P) and surface area (S) values of all SCLF hexaferrite samples

Sample name	Density (g/cm ³)		Porosity (P) (%)	$S \times 10^7$ (cm ² /g)
	XRD (ρ_x)	Bulk (ρ_{bulk})		
SCLF 1	5.18	3.03	41.50	23.37
SCLF 2	5.20	2.75	47.11	25.73
SCLF 3	5.22	2.52	51.72	26.97
SCLF 4	5.25	2.20	58.09	27.90
SCLF 5	5.27	2.95	44.02	28.44
SCLF 6	5.27	2.90	44.97	29.88

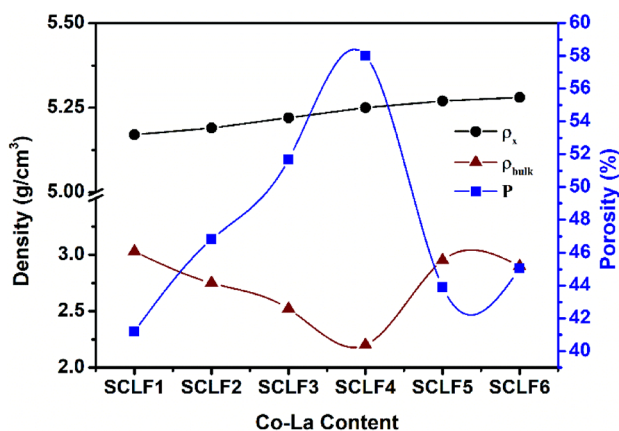


Fig. 5 Variation of density and porosity with different levels of Co–La substitution

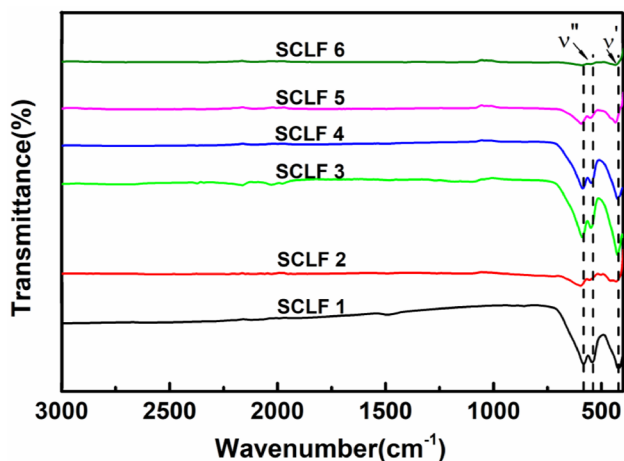


Fig. 6 FTIR spectra in 400–3000 cm⁻¹ range of all SCLF hexaferrite samples

4.4 SEM and EDAX analysis

Figure 7 shows micrographs of all prepared SCLF hexaferrite samples. The formation of grains exhibiting

Table 4 FTIR spectra details of all SCLF hexaferrite samples

Sample name	Fe–O vibrations at	
	Octahedral sites (400–450 cm ⁻¹)	Tetrahedral sites (500–600 cm ⁻¹)
SCLF 1	422.35	541.92 582.42
SCLF 2	430.06	555.42 584.35
SCLF 3	426.20	547.70 588.20
SCLF 4	426.20	547.70 586.27
SCLF 5	433.92	551.26 593.99
SCLF 6	433.92	– 590.13

diverse sizes and shapes can be attributed to the aggregation of crystallites caused by dipolar attractive interaction among magnetic particles. It is evident from Fig. 7 that the substitution of Co²⁺–La³⁺ ions improve the inter-grain connectivity of particles. All the compositions obtained display a porous morphology and consist of micron-sized agglomerates containing a substantial number of nanometer-sized particles [36]. As the proportion of substituents increases in the composition of the synthesized samples, there is no significant change in morphology, which is associated with the same synthesis conditions in all SCLF samples. It should be noted that, in comparison with traditional methods of obtaining hexaferrite, this sol–gel technique made it possible to obtain samples with a more developed morphology.

Elemental analysis performed by the method of energy-dispersive analysis (Fig. 8) confirms that all obtained powders correspond in their composition to the calculated values within the error of the determination method. In addition, it was found that all the main chemical elements are evenly distributed over the entire area of the samples, which indirectly confirms the XRD phase analysis data on the homogeneous nature of the compositions obtained.

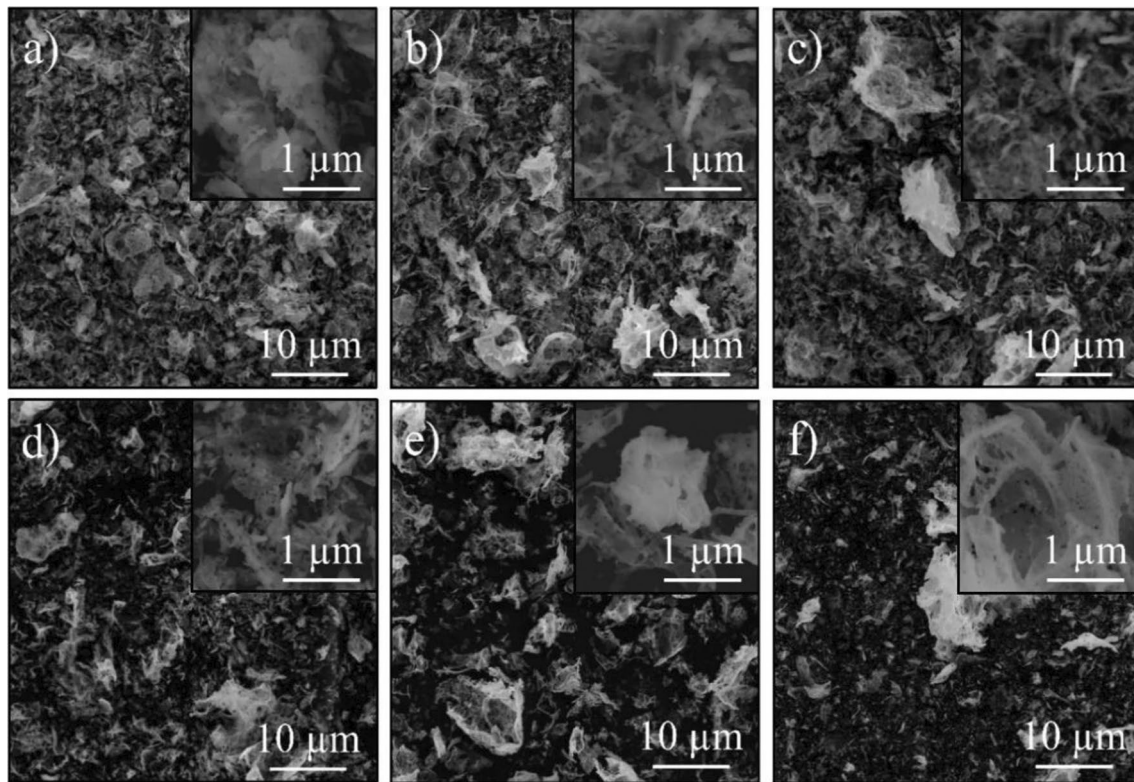


Fig. 7 SEM micrographs of the SCLF 1 (a) SCLF 2 (b) SCLF 3 (c) SCLF 4 (d) SCLF 5 (e) and SCLF 6 (f) hexaferrite samples

4.5 Mössbauer spectra analysis

Figure 9 shows the ^{57}Fe Mössbauer spectra obtained at room temperature of strontium hexaferrite doped with various amounts of cobalt and lanthanum cations. All spectra show five well-defined sextets of iron cations, which ascribed the structural positions of magnetoplumbite, i.e., octahedral, tetrahedral, and trigonal bipyramidal iron positions. The parameters of the quadrupole splitting, isometric shift, and hyperfine field are listed in Table 5. The obtained values are in harmony with the results of earlier published works on strontium hexaferrite [37].

It is known that in pure strontium hexaferrite, the area of the sextet is directly related to the Fe^{3+} cations in the corresponding sites and is equal to the ratio $12\text{k}-50$, $4\text{f}_1-16.7$, $4\text{f}_2-16.7$, $2\text{a}-8.3$, $2\text{b}-8.3$ [38–40]. Based on the relative area of SCLF1 (pure SrM), the positions of 4f_2 , 12k , and 2a are quite close to their predicted values, while the 4f_1 site is heavily populated and the 2b site has less occupancy, as seen in Table 5. Figure 10 illustrates the dependence of the Fe^{3+} ion concentration and degree of substitution at the 2a , 12k , 2b , 4f_1 , and 4f_2 sites. The relative area of SCLF samples

changes from SCLF1 (48.7:21.5:17.7:6.1:3.3) to SCLF6 (43.5:27.5:17.5:3.6:3.5) and is ascribed to the substitution Co^{2+} and La^{3+} ions over five crystallographic sites. Moreover, from SCLF 3 to SCLF 4, the total relative area of 12k and 2a sites decreases by 21.86% and that of the 4f_2 site by 19%, signifying the tendency of the substituents to occupy these sites. On the other hand, the relative area of 4f_1 increases by 34%, indicating that some of the Fe ions migrated towards the 4f_1 site from SCLF 3 to SCLF 4. According to Eq. 10, M_a decreases with the occupancy of weak magnetic Co^{2+} ($3 \mu_B$) and diamagnetic La^{3+} ($0 \mu_B$) ions on 12k and 2a sites, while M_b increases with the increases in area/occupancy of 4f_1 site by Fe^{3+} ions. However, the decrease in the net area observed at $12\text{k}-2\text{a}$ spin-up sites is greater than the increase in the net area of the 4f_1 and 4f_2 spin-down sites, which may indicate that relatively large no. of $\text{Co}^{2+}-\text{La}^{3+}$ ions occupy the $12\text{k}-2\text{a}$ sites from SCLF 3 to SCLF 4. Therefore, net magnetic moment or $M = M_a - M_b$ decreases considerably in SCLF 4.

The isomer shift (IS) provides information about the chemical bonding, including the valence state of Fe^{3+} ions in magnetically ordered materials. From the previous reports, the value of isomer shift for Fe^{2+} ,

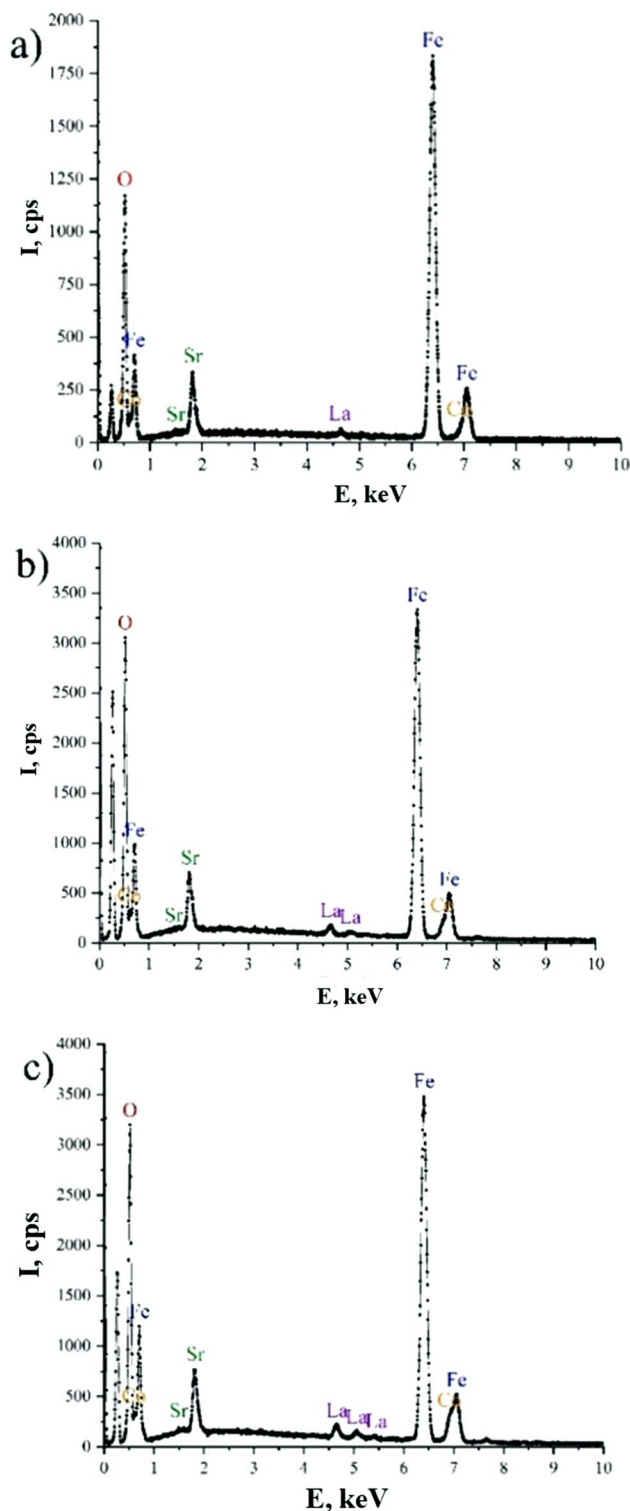


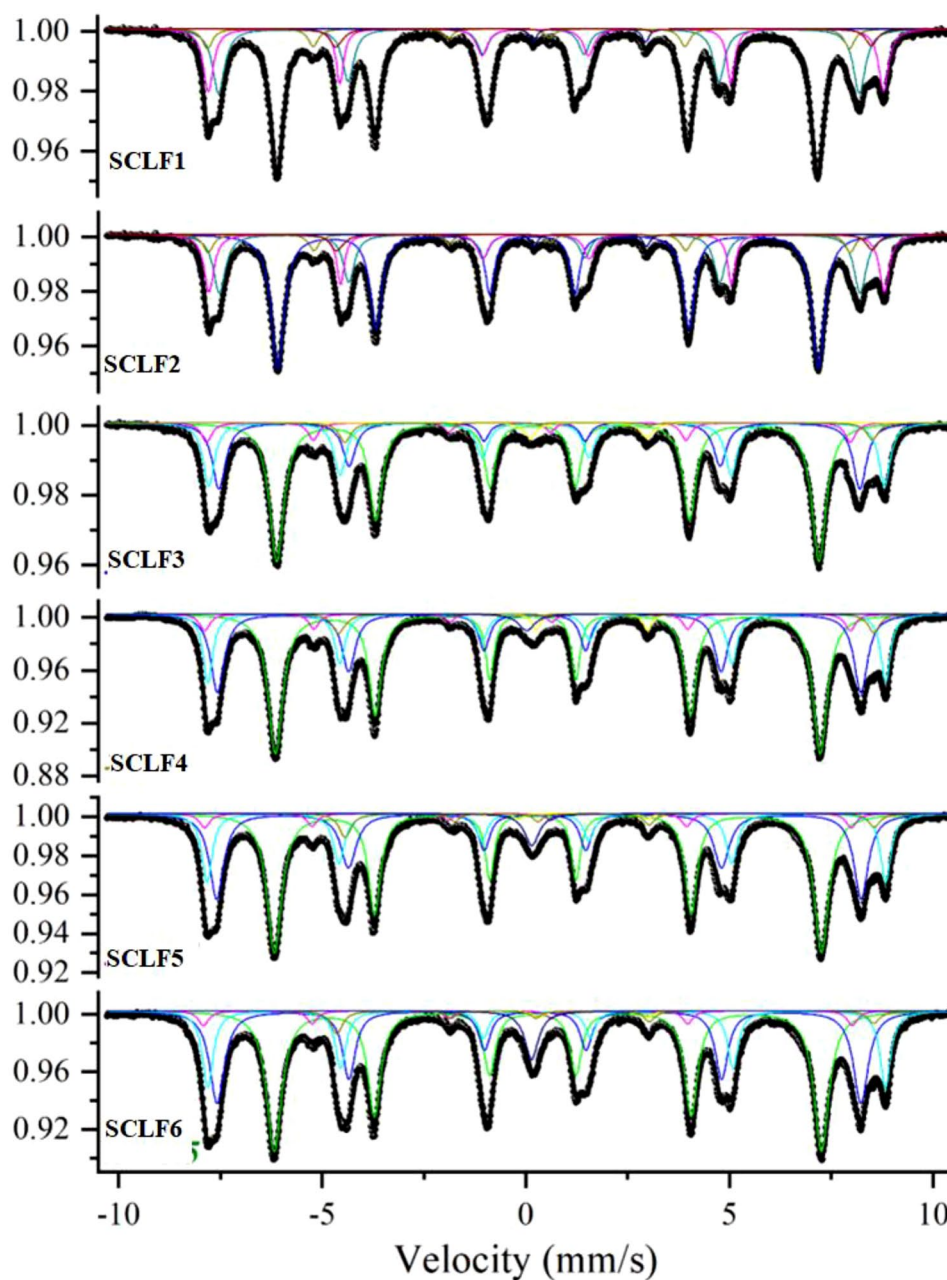
Fig. 8 EDX spectra of the SCLF 2 (a), SCLF 4 (b), and SCLF 6 (c) samples

Fe^{3+} , and Fe^{4+} ions should lie between 0.6 to 1.7 mm/s, 0.05 to 0.5 mm/s, and 0.15 to 0.05 mm/s respectively. Table 5 displays the value of isomer shift ranges from 0.27 to 0.38 mm/s, identifying that samples consist of Fe^{3+} high spin valence state. With substitution, the isomer shift value remains relatively constant for all crystallographic sites, suggesting little impact on the s electron density of Fe^{3+} ions. The quadrupole splitting gives knowledge about the local distortion and symmetry of the crystal lattice. Substitution of Co–La ions causes a feeble reduction in the QS value of $4f_1$ and $4f_2$, implying a minor perturbation of the symmetry in the vicinity of these sites. It can be noted that the values of the hyperfine field (ranging from 40.2 to 41.05 mm/s) and quadrupole splitting (in the order of 2.5–2.8 mm/s) for site 2b may indicate a strong deformation of the local lattice medium with Co^{2+} – La^{3+} substitution [41]. The above discussion highlights that the magnetic parameters of all the SCLF samples are strongly associated with the arrangement of substituents across five crystallographic sites. The vacancies resulting in the replacement of Fe^{3+} ions by Co^{2+} – La^{3+} ions may serve as effective pinning centers for domain walls. This magnetic dilution is demonstrated by the decrease observed in H_c and M_s values as shown in Table 7, which will be discussed further in the subsequent section on magnetic analysis (Fig. 11).

4.6 Magnetic analysis

The magnetic characteristics of the prepared specimens can be tailored by substituting cations with varying electronegativity, magnetic moment, and d-configuration [42]. It has been reported that ions with higher electronegativity generally occupy more octahedral sites than tetrahedral positions of the crystal lattice [43]. The electronegativity of La^{3+} (1.1) ions are lower than that of Co^{2+} (1.88) ions, so the former ions tend to occupy the tetrahedral site $4f_1$ (\downarrow) [44]. According to ligand field theory, La^{3+} ions have no site preference due to d^0 configuration and Co^{2+} ions with d^7 configuration preferably choose to occupy octahedral sites $12k$ (\uparrow), $2a$ (\uparrow), $4f_2$ (\downarrow) [45, 46]. When the substituted ion has larger ionic radii than the host ion, it preferentially occupies octahedral sites at the edges of the unit cell. From previous reports Co^{2+} ($3\mu_B$) ions can occupy both the octahedral ($4f_2$) and tetrahedral ($4f_1$) crystallographic sites [47], while La^{3+} ($0\mu_B$) behaves as a non-magnetic ion and can occupy more octahedral spin-up positions ($12k$ and $2a$) than tetrahedral sites

Fig. 9. ^{57}Fe Mössbauer spectra of all SCLF hexaferrite samples



[48] The saturation magnetization (M_s), remanence magnetization (M_r), coercivity (H_c), anisotropy field (H_a), remanence ratio (M_r/M_s) and magnetic moment (n_B) values derived from the M - H loop are listed in Table 7. Figure 12a demonstrates the hysteresis loops of all SCLF samples at room temperature. The values of M_s and H_a parameters decrease from SCLF1 to SCLF 4 samples, followed by a gradual increase.

The saturation law is used to derive the M_s and H_a of prepared specimens using the below equation [49]:

$$M = M_s(1 - A/H - B/H^2) + \chi_p H \quad (8)$$

Here M_s imply as saturation magnetization, χ_p illustrates susceptibility at a high field, A represents an inhomogeneity parameter, and B represents the anisotropy parameter.

In the hexagonal symmetry of the crystal, we can calculate B using the below expression:

$$B = H_a^2/15 = 4K_1^2/15M_s^2 \quad (9)$$

Table 5 Isometric shift, hyperfine field, and quadrupole splitting of spectral components of all SCLF hexaferrite samples

Sample name	Site	IS (mm/s)	QS (mm/s)	H_{eff} (mm/s)	Area (%)
SCLF 1	12k	0.34(9)	0.38(3)	41.17(1)	48.7(3)
	4f1	0.27(2)	0.13(7)	48.85(4)	21.5(3)
	4f2	0.38(1)	0.26(4)	51.45(3)	17.7(4)
	2a	0.28(2)	0.73(1)	48.93(5)	6.1(8)
	2b	0.60(4)	2.60(3)	40.80(0)	3.3(7)
	Doublet	1.56(8)	2.75(5)	–	1.1(5)
SCLF 2	12k	0.35(3)	0.38(2)	41.22(7)	49.2(6)
	4f1	0.27(4)	0.13(4)	48.85(7)	22.0(0)
	4f2	0.38(2)	0.26(0)	51.50(0)	17.9(2)
	2a	0.27(8)	0.72(0)	48.96(2)	6.3(0)
	2b	0.62(6)	2.59(1)	40.86(7)	3.2(7)
	Doublet	1.57(8)	2.76(1)	–	1.2(5)
SCLF 3	12k	0.35(5)	0.37(2)	41.35(1)	48.3(0)
	4f1	0.27(4)	0.11(7)	48.86(9)	19.5(6)
	4f2	0.37(7)	0.27(1)	51.53(3)	21.3(3)
	2a	0.28(8)	0.70(5)	49.09(1)	5.6(1)
	2b	0.66(7)	2.73(3)	40.22(2)	2.9(6)
	Doublet	1.54(1)	2.85(5)	–	2.2(4)
SCLF 4	12k	0.35(6)	0.36(8)	41.53(8)	45.5(0)
	4f1	0.27(5)	0.10(5)	49.06(2)	26.2(5)
	4f2	0.38(2)	0.26(4)	51.67(6)	17.2(0)
	2a	0.28(6)	0.65(3)	49.23(6)	4.7(5)
	2b	0.68(0)	2.57(3)	40.85(5)	3.0(5)
	Doublet	1.61(7)	2.73(9)	–	1.6(2)
SCLF 5	12k	0.35(7)	0.37(0)	41.71(6)	43.6(7)
	4f1	0.27(3)	0.09(4)	49.14(9)	27.6(9)
	4f2	0.36(9)	0.26(9)	51.76(0)	17.5(7)
	2a	0.29(6)	0.70(0)	49.32(4)	3.8(0)
	2b	0.67(8)	2.80(2)	40.26(3)	4.0(2)
	Doublet	1.39(2)	3.15(3)	–	0.5(9)
SCLF 6	12k	0.35(5)	0.37(0)	41.73(9)	43.5(7)
	4f1	0.27(7)	0.08(9)	49.09(8)	27.5(5)
	4f2	0.38(9)	0.23(8)	51.68(0)	17.5(4)
	2a	0.29(1)	0.68(5)	49.48(1)	3.6(3)
	2b	0.57(4)	2.73(0)	41.05(1)	3.5(1)
	Doublet	1.63(7)	2.65(8)	–	0.7(4)
SCLF 6	Singlet	0.14(2)	–	–	3.4(6)

Here K_1 denotes a constant of anisotropy and H_a implies an anisotropy field. The $M-H$ loop in Fig. 12a demonstrated a rapid increment in M_s at a low applied field which gets slow at a high applied field and a linear relationship is observed for all prepared specimens.

Now, A/H and χ_p terms can be eliminated from Eq. 8, and we can calculate the B term from the slope of a straight line, ($M = M_s(1-B/H^2)$ versus $1/H^2$) as shown in Fig. 11. Subsequently, by putting the calculated B value in Eq. 9, H_a can be determined. The magnetic moment of the incorporated specimen can be explained through the distribution of host and

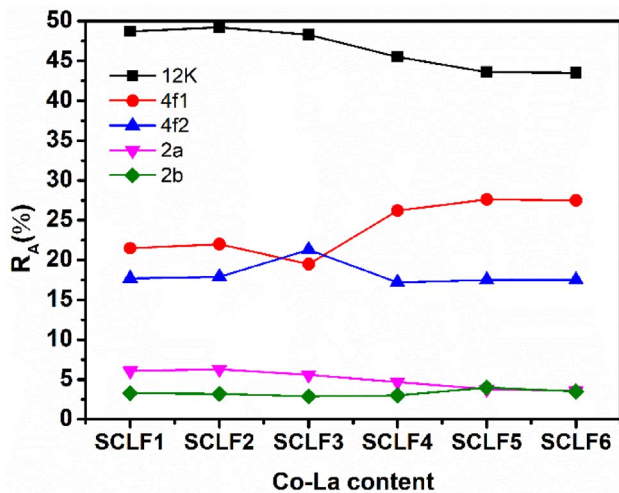


Fig. 10 The relative area of Fe³⁺ ions on Co–La level of substitution at the position 12k, 2a, 2b, 4f1 and 4f2

substituted cations over five crystallographic sites of hexagonal crystal structure using the following expression [50]:

$$M_s = M_a(2a + 12k + 2b)(\uparrow) - M_b(4f_1 + 4f_2)(\downarrow) \quad (10)$$

The total magnetization increases by substituting non-magnetic ions or less magnetic at the (4f_{1↓} + 4f_{2↓}) lattice site, while magnetization shows decline behavior with the substitution of these ions at (2a ↑ + 12k ↑ + 2b ↑) lattice sites [51].

Table 7 shows that M_s decreases non-monotonically with increasing the level of substitution from SCLF 1 to SCLF 6. The decrease in M_s can be described by various factors, such as spin canting, change of valence state from high to low spin, site occupancy, and exchange interaction [52]. For lower levels of substitution (SCLF 1 to SCLF 3), a 14% decrease in the M_s value is evident. This decrease can be attributed to the replacement of Fe³⁺ (5 μ_B) ions by non-magnetic (La³⁺) and weakly magnetic (Co²⁺) cations, which reduces the number of Fe³⁺ ions on spin-up positions. This resulted in the conversion of Fe³⁺ ions to Fe²⁺ ions to maintain electrical neutrality, which reduces the strength of the superexchange interactions and leads to a decline in magnetic moment. Moreover, the decrease in M_s from SCLF 3 to SCLF 4 is about 23%, which is consistent with the 21% decrease observed in the relative area of the 12k-2a sites in the Mössbauer analysis. This indicates that the Co²⁺–La³⁺ ions replace more no. of Fe³⁺ ions of 12k and 2a sites than other positions

[53]. Thereafter an increase of 37% in M_s from SCLF 4 to SCLF 6, can be ascribed as a reduction in porosity. The Porosity acts as a non-magnetic void, which depresses magnetization and simultaneously induces demagnetizing fields. However, the increase in M_s is not as substantial as the decrease in porosity. This can be explained by the fact that the increase in M_s also depends on the occupation of 4f₂ and 4f₁ positions of crystallographic sites [54]. Furthermore, the substitution of a rare-earth element in the ferrite attributes to cationic vacancies disturbs the collinear ferromagnetic order and causes environmental distortions [55]. In this context, doping with rare-earth cations often leads to incomplete substitution [56, 57], which may indirectly explain the significant change in the intensity of the diffraction peaks of the SCLF 6 sample and the absence of a large difference between the Mössbauer spectra of the SCLF 5 and SCLF 6 samples.

The highest values of the coercivity (5026 Oe), and remanent magnetization (52.68 emu/g) are observed in a pure sample of strontium hexaferrite (SCLF 1), which is associated with the absence of substituent cations in the crystal lattice. The behavior of H_c can be easily explained by intrinsic and extrinsic factors. Intrinsic factors are those that are inherent to the material, such as the crystal structure, chemical composition, and anisotropy field (H_a) [58]. External factors are those that are external to the material such as temperature, magnetic field, and grain size [59]. The initial fall observed in H_c from SCLF 1 (5026 Oe) to SCLF 4 (2730 Oe) with increasing the level of substitution, is caused by H_a . The anisotropy field (H_a) depends primarily on the magnetic moments of the iron ions at the 4f₂ and 2b sites. A larger anisotropy field leads to a higher coercivity, i.e., more energy is required to reverse the magnetic moment of the hexaferrite. However, with further substitution at SCLF 5 and SCLF 6, H_c gradually decreases to 839 Oe and H_a remains relatively constant. This envisaged behavior can be explained through the existence of inter-grain connectivity in SCLF5 and SCLF6 samples as seen in SEM images. The remanent magnetization (M_r) depends on the orientation of the magnetic moments and decreases from SCLF 1 (52.68 emu/g) to SCLF 6 (32.27 emu/g) with increasing the level of substitution, as seen in Fig. 13 (b).

The remanence ratio (M_r/M_s) is a measure of the retention of magnetization after removing an applied field, and it's usually high in M-type hexaferrite,

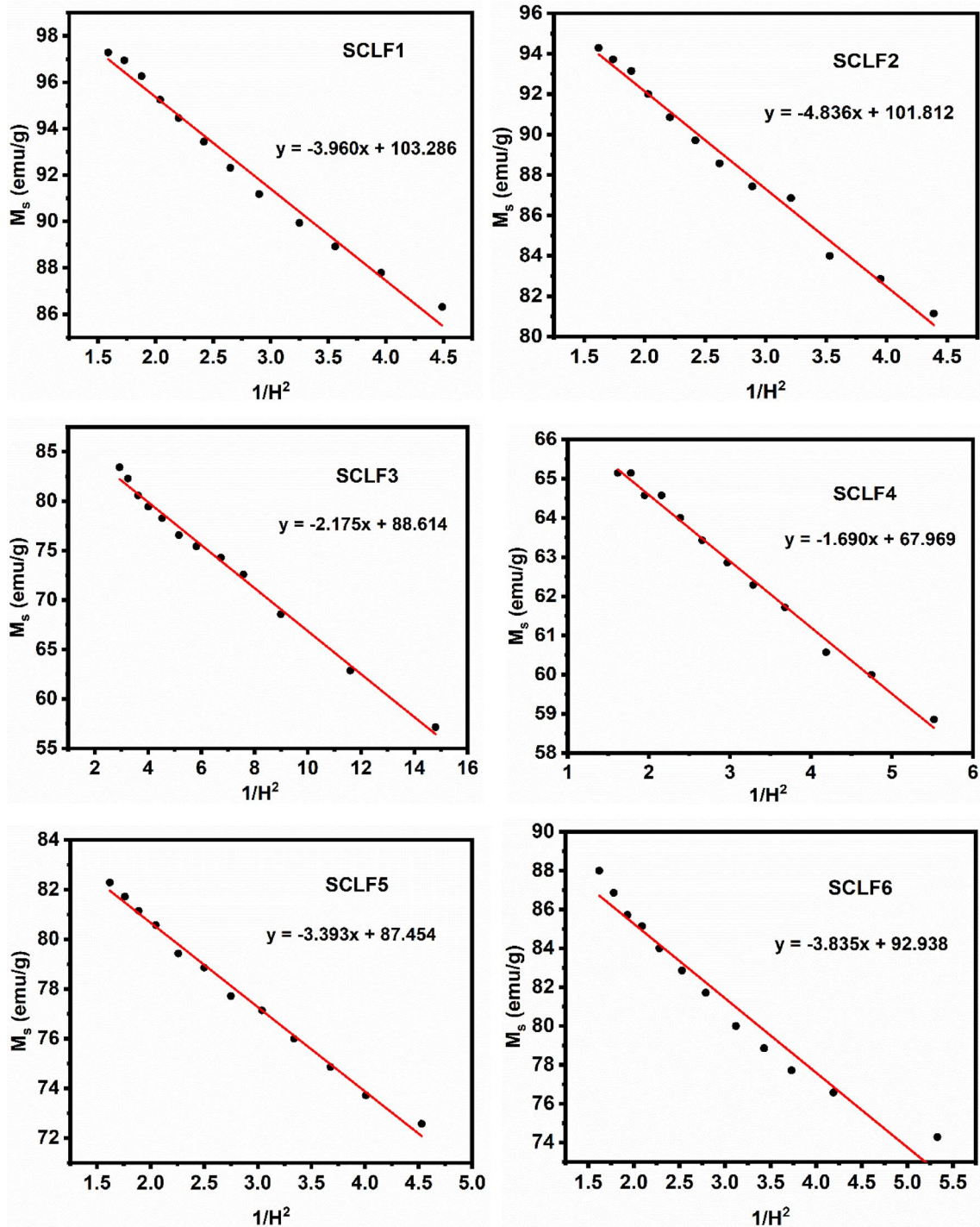


Fig. 11 M_s versus $1/H^2$ plots for all SCLF hexaferrite samples

indicating high remanence. This ratio is also used to determine the formation of the inter-grain group and magnetic hardness of the material and its value should be in the range of 0 to 1 [60]. The magnetic material whose values lie within 0.05 to 0.5 is considered to be

randomly oriented multi-domain particles [61]. It is seen in Table 6 that the remanence value of all prepared specimens comes out to be less than or equal to 0.5 which proves the formation of multi-domain particles in all SCLF samples [62].

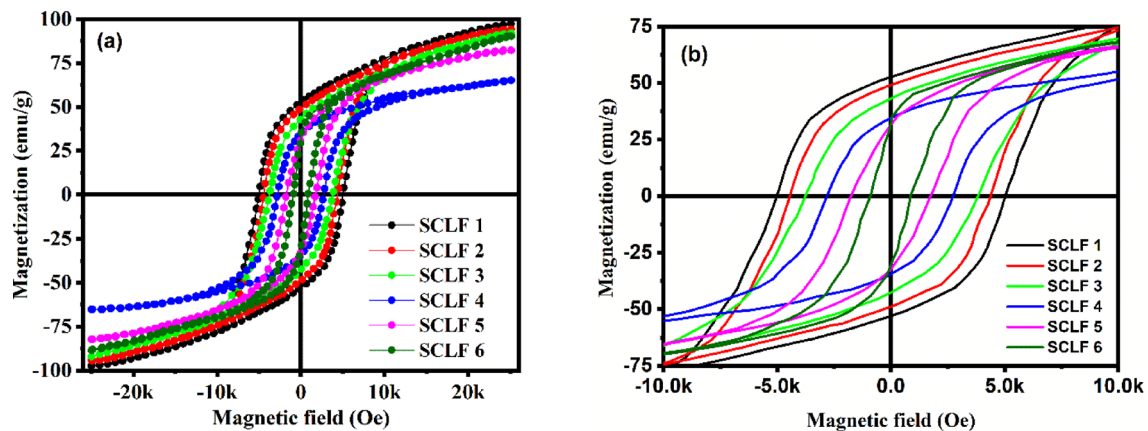


Fig. 12 Survey (a) and enlarged (b) Hysteresis loops of all SCLF hexaferrite

The Bohr magneton (n_B) shows a significant role in investigating the magnetic characteristics of the material, which is widely used in microwave and high-frequency applications and calculated using the following Equation:

$$n_B = \frac{M_s \times M.W}{5585} \quad (11)$$

The Bohr magneton is closely related to saturation magnetization and molecular weight ($M.W$). As the level of substitution increases, the value of the Bohr magneton decreases, potentially weakening the magnetic interactions within the hexaferrite. This can be observed in Table 7.

The term dM/dH represents magnetic susceptibility and it plays an indispensable role in determining the magnetic characteristics of the material. By analyzing the height and shape of the dM/dH peaks, it is possible to depict the size and distribution of the magnetic domains in the material [63]. Figure 14 displays the dM/dH versus H curves for all SCLF samples, which shows an asymmetric peak around $H \rightarrow 0$ with a separation of $2H_m$. The values of H_m and dM/dH (at $H \rightarrow 0$ and $H \rightarrow H_m$) resulting from the dM/dH versus H plots are listed in Table 7. It has been reported that a single domain particle possesses a square-shaped M-H loop and it exhibits a high dM/dH value for the coercive field (H_c) and zero (0) for $H \rightarrow 0$ [64]. Some finite value of dM/dH at $H \rightarrow 0$ for all SCLF samples affirms the existence of a multi-domain and a single-domain/pseudo-domain regime. The curves of dM/dH versus H showed peaks at H_m , with a larger peak height at H_m than at $H \rightarrow 0$. For SCLF 1, SCLF 3, SCLF 4, and SCLF 5, the values

of H_m are greater than H_c , which can be attributed to the presence of a switching field distribution [65]. This could also indicate that the magnetic domain within the material is well-ordered and aligned in the same direction. This results in a higher magnetic susceptibility, which leads to a high degree of magnetic ordering and stability. This type of magnetic ordering may be desirable for applications where magnetic materials are used as high-performance magnetic components [66].

In SCLF 2 and SCLF 6 the H_m value is less than H_c , which may indicate the presence of superparamagnetic domains in the material, that are highly unstable and susceptible to thermal fluctuations. From Fig. 14, it can be seen that the separation between the peaks of dM/dH curves gradually decreases as the level of substitution increases. This reduction in peak separation may be due to changes in the magnetic properties of the material caused by the Co–La substitution, leading to a reduction in the difference between the magnetic domains within the material [67]. This may lead to a decrease in the stability of the magnetic domains, resulting in a narrower separation between the peaks in the dM/dH curves. However, in SCLF 6, multiple peaks are observed in the dM/dH vs H curves, which may indicate the complex magnetic behavior of the material and need further investigation to determine the exact reason. For recording media applications, both saturation magnetization and coercivity should be high enough to ensure that the recorded magnetic signals are strong and stable. Table 8 depicts that the substitution of Co–La ions enhances saturation magnetization with tunable coercivity than the reported results, which is suitable for recording media

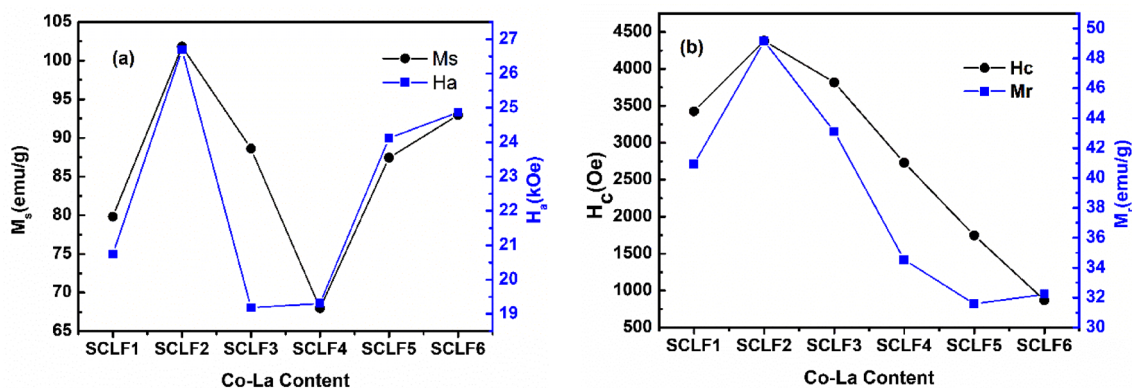


Fig. 13 Variation of M_s and H_a (a) H_c and M_r (b) with different level of La–Co substitution

Table 6 Magnetic parameters M_s , H_c , H_a , M_r and M_r/M_s value of all SCLF hexaferrite samples

Sample name	M_s (emu/g)	H_c (Oe)	H_a (kOe)	M_r (emu/g)	M_r/M_s
SCLF 1	103.290	5026.54	23.98	52.68	0.510
SCLF 2	101.812	4379.59	26.69	49.18	0.483
SCLF 3	88.614	3826.72	19.18	43.14	0.486
SCLF 4	67.969	2728.33	19.31	34.57	0.508
SCLF 5	87.454	1741.77	24.12	31.61	0.361
SCLF 6	92.939	862.47	24.87	32.27	0.347

Table 7 Calculated values of n_B , H_m , dM/dH at $H \rightarrow 0$ and $H \rightarrow H_m$ values of all SCLF hexaferrite samples

Sample name	n_B (μ_B)	H_m (Oe)	$dM/dH \times 10^{-3}$ (emu/g. Oe)	
			$H \rightarrow 0$	$H \rightarrow H_m$
SCLF 1	7.27	5622	3.24	34.42
SCLF 2	19.43	3554	4.07	39.22
SCLF 3	16.99	4016	5.36	24.67
SCLF 4	13.08	2852	5.86	29.53
SCLF 5	16.91	2501	14.69	32.17
SCLF 6	18.05	641	41.28	53.93

applications. It is also evident from magnetic susceptibility results that SCLF1, SCLF3, SCLF4, and SCLF5 exhibit a high degree of magnetic stability which is also a desirable property of recording media.

5 Conclusion

Cobalt- and Lanthanum-substituted $\text{SrCo}_{1.5z}\text{La}_{0.5z}\text{Fe}_{12-2z}\text{O}_{19}$ hexaferrites were successfully synthesized by the sol-gel auto-combustion technique. Substitution does not alter the magnetoplumbite structure of M-type hexaferrite, as displayed in XRD analysis. The insertion of Co–La ions improves the inter-grain connectivity of hexagonal grains. The VSM analysis reveals the maximum value of saturation magnetization (103.29 emu/g) and coercivity (5026.24 Oe) in the SCLF1 sample. The tendency of Co–La ions to occupy particular lattice sites of crystal structure causes a non-linear decrement in saturation magnetization from 103.29 to 67.96 emu/g and a gradual decrease in coercivity from 5026.24 Oe to 862.47 Oe. Mössbauer’s analysis supports the magnetic results and results of dM/dH curves affirm good magnetic ordering and stability in SCLF1, SCLF3, SCLF4, and SCLF5 samples, which is an indispensable property of recording media applications.

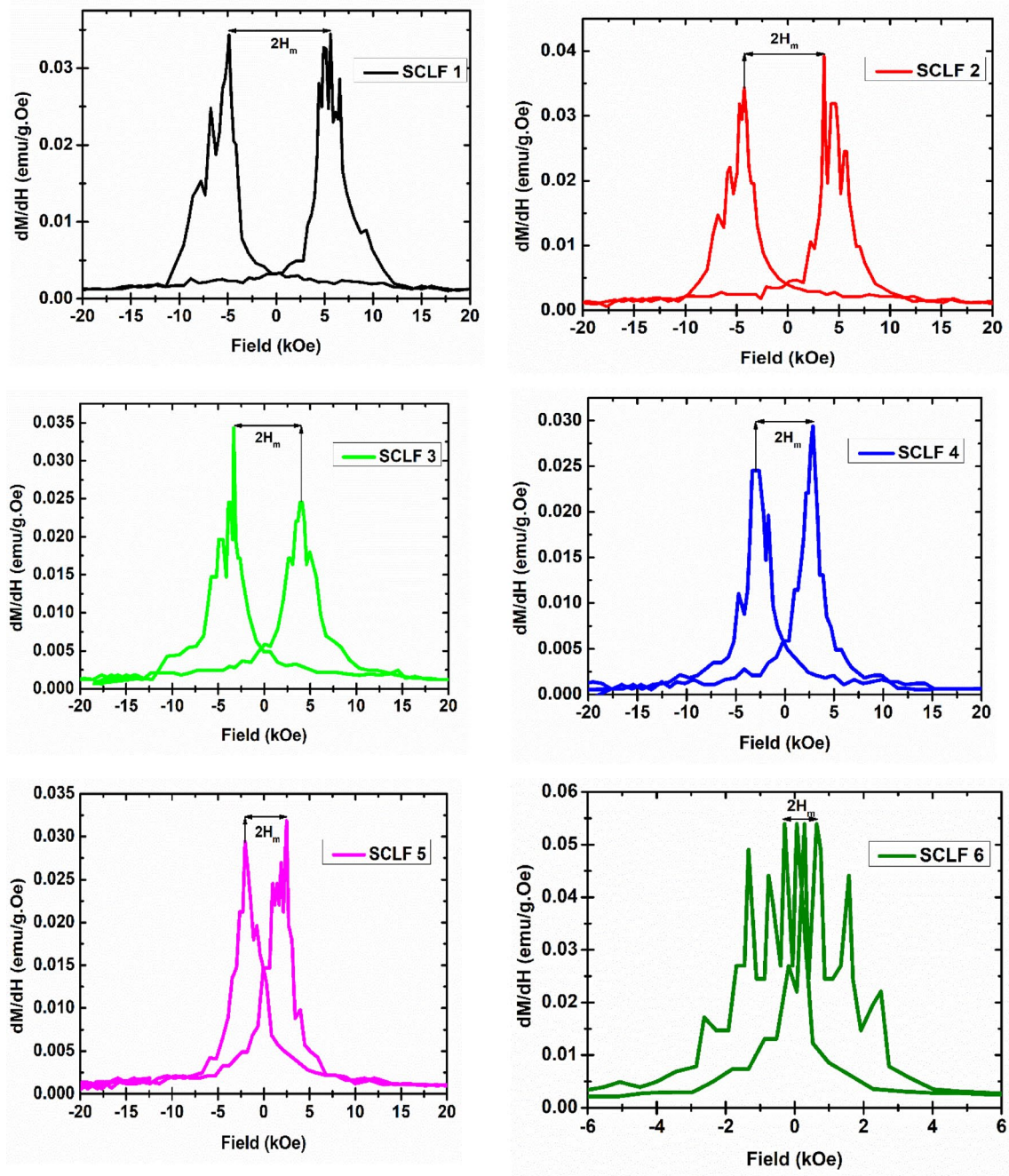


Fig. 14 dM/dH versus H curves of all SCLF hexaferrite samples

Table 8 Summary of Reported magnetic parameters of doped SrM hexaferrite

S. No	Method	Material	M_s (emu/g)	H_c (Oe)	References
1	Citrate precursor method	La-doped SrM hexaferrite	49.77–32.46	5597–6326	[68]
2	Sol-gel method	La-Zn-doped SrM hexaferrite	63.26–66.20	–	[69]
3	Ultrasonic spray pyrolysis method	Ca-La-Co-doped SrM hexaferrite	72.83–60.42	7880–7035	[70]
4	Citrate precursor method	La-Mg-doped SrM hexaferrite	68–51	6389–5399	[71]
5	Precursor synthesis	La-doped SrM hexaferrite	57.6–47.63	1874–375	[20]
6	Sol-gel auto-combustion method (present work)	Co-La-doped SrM hexaferrite	103.2–67.96	5026–862	–

Author contributions

MT: Investigation, Formal analysis, Data curation, Writing—original draft, Data analysis and Curation, Software, Original Drafting. CS: Conceptualization, Investigation, Methodology, Data Curation, Writing—review and editing. AKS: Investigation, Data Analysis. SRM and MFA: Performed XRD and FTIR Characterization. KDM, IVB, VGS, VIP: Performed SEM, Mössbauer and VSM Measurements.

Funding

There are not any financial and personal relationships with other people or organisations that could be viewed as inappropriately influencing (bias) their work. Funding source(s) had no such involvement in the collection, analysis and interpretation of data; in the writing of the report.

Data availability

The datasets generated during and/or analyzed during the current study are available from the corresponding author on reasonable request.

Declarations

Conflict of interest There are no potential conflicts of interest.

References

1. H. Bayrakdar, Fabrication, magnetic and microwave absorbing properties of $\text{Ba}_2\text{Co}_2\text{Cr}_2\text{Fe}_{12}\text{O}_{22}$ hexagonal ferrites. *J. Alloys Compd.* **674**, 185–188 (2016). <https://doi.org/10.1016/j.jallcom.2016.03.055>
2. A. Sharbati, J. Mola-Verdi-Khani, G.R. Amiri, Microwave absorption studies of nanocrystalline $\text{SrMn}_{x/2}(\text{TiSn})_{x/4}\text{Fe}_{12-x}\text{O}_{19}$ prepared by the citrate sol-gel method. *Solid State Commun.* **152**(3), 199–203 (2012). <https://doi.org/10.1016/j.ssc.2011.11.009>
3. A.D. Deshpande, K.G. Rewatkar, V.M. Nanoti, Study of morphology and magnetic properties of nanosized particles of Zirconium—Cobalt substituted calcium hexaferrites. *Mater. Today Proc.* **4**(11), 12174–12179 (2017). <https://doi.org/10.1016/j.matpr.2017.09.147>
4. G. Feng et al., Co substituted $\text{BaFe}_{12}\text{O}_{19}$ ceramics with enhanced magnetic resonance behavior and microwave absorption properties in 2.6–18 GHz. *Ceram. Int.* **45**(11), 13859–13864 (2019). <https://doi.org/10.1016/j.ceramint.2019.04.083>
5. B. Zong, X. Niu, Analysis of structure and magnetic behavior in M-type hexaferrite compounds $\text{Sr}_{1-x}\text{Y}_x\text{Fe}_{10}\text{CoTiO}_{19}$. *J. Mater. Sci. Mater. Electron.* **31**(7), 5290–5297 (2020). <https://doi.org/10.1007/s10854-020-03089-0>
6. Y. Feng, S. Li, Y. Zheng, Z. Yi, Y. He, Y. Xu, Preparation and characterization of MgFe_2O_4 nanocrystallites via PVA sol-gel route. *J. Alloys Compd.* **699**, 521–525 (2017). <https://doi.org/10.1016/j.jallcom.2016.12.432>
7. S.K. Durrani, S. Naz, M. Mehmood, M. Nadeem, M. Siddique, Structural, impedance and Mössbauer studies of magnesium ferrite synthesized via sol-gel auto-combustion process. *J. Saudi Chem. Soc.* **21**(8), 899–910 (2017). <https://doi.org/10.1016/j.jscs.2015.12.006>
8. S.V. Trukhanov et al., Magnetic and dipole moments in indium doped barium hexaferrites. *J. Magn. Magn. Mater.* **457**, 83–96 (2018). <https://doi.org/10.1016/j.jmmm.2018.02.078>

9. R.B. Jotania, R.B. Khomane, C.C. Chauhan, S.K. Menon, B.D. Kulkarni, Synthesis and magnetic properties of barium-calcium hexaferrite particles prepared by sol-gel and microemulsion techniques. *J. Magn. Magn. Mater.* **320**(6), 1095–1101 (2008). <https://doi.org/10.1016/j.jmmm.2007.10.032>
10. C. Singh, S. Bindra Narang, I.S. Hudiara, K.C. James Raju, K. Sudheendran, Microwave and electrical properties of Co–Zr substituted Ba–Sr ferrite. *J. Ceram. Process. Res.* **11**(6), 692–697 (2010)
11. T. Giannakopoulou, L. Kompotiatis, A. Kontogeorgakos, G. Kordas, Microwave behavior of ferrites prepared via sol–gel method. *J. Magn. Magn. Mater.* **246**(3), 360–365 (2002). [https://doi.org/10.1016/S0304-8853\(02\)00106-3](https://doi.org/10.1016/S0304-8853(02)00106-3)
12. N. Tran, Y.J. Choi, T.L. Phan, D.S. Yang, B.W. Lee, Electronic structure and magnetic and electromagnetic wave absorption properties of $\text{BaFe}_{12-x}\text{Co}_x\text{O}_{19}$ M-type hexaferrites. *Curr. Appl. Phys.* **19**(12), 1343–1348 (2019). <https://doi.org/10.1016/j.cap.2019.08.023>
13. G. Sriramulu, N. Maramu, K. Praveena, S. Katlakunta, Effect of Cr^{3+} – Al^{3+} cosubstitution on structural, magnetic and microwave absorption properties of Srhexaferrites. *J Mater Sci Mater Electron.* **33**(35), 26113–26123 (2022). <https://doi.org/10.1007/s10854-022-09298-z>
14. J. Du, L. Lian, Y. Liu, Y. Du, Effect of Zn substitution on the structure and magnetic properties of $\text{Sr}_{0.1}\text{La}_{0.45}\text{Ca}_{0.45}\text{Fe}_{11.7-x}\text{Zn}_x\text{Co}_{0.3}\text{O}_{19}$ hexagonal ferrites. *J Mater Sci Mater Electron.* **30**(21), 19618–19624 (2019). <https://doi.org/10.1007/s10854-019-02335-4>
15. X. Suo, J. Li, W. Zhang, P. Li, Effect of La_{3+} Substitution on the Structure and Magnetic Properties of M-type Sr Hexaferrites. *J Supercond Nov Magn.* **36**(1) 197–206 (2023). <https://doi.org/10.1007/s10948-022-06450-y>
16. R.A. Nandotaria et al., Magnetic interactions and dielectric dispersion in Mg substituted M-type Sr–Cu hexaferrite nanoparticles prepared using one step solvent free synthesis technique. *Ceram. Int.* **44**(4), 4426–4435 (2018). <https://doi.org/10.1016/j.ceramint.2017.12.043>
17. M.A. Almessiere, Y. Slimani, H. Güngüneş, A. Baykal, S.V. Trukhanov, A.V. Trukhanov, Manganese/yttrium codoped strontium nanohexaferrites: evaluation of magnetic susceptibility and mossbauer spectra. *Nanomaterials* (2019). <https://doi.org/10.3390/nano9010024>
18. B.K. Rai, S.R. Mishra, V.V. Nguyen, J.P. Liu, Synthesis and characterization of high coercivity rare-earth ion doped $\text{Sr}_{0.9}\text{RE}_{0.1}\text{Fe}_{10}\text{Al}_2\text{O}_{19}$ (RE: Y, La, Ce, Pr, Nd, Sm, and Gd). *J. Alloys Compd.* **550**, 198–203 (2013). <https://doi.org/10.1016/j.jallcom.2012.09.021>
19. C.C. Chauhan, T. Gupta, A.A. Gor, K.R. Jotania, R.B. Jotania, Effect of calcination temperature on structural and magnetic properties of lightly lanthanum substituted M-type strontium cobalt hexaferrites. *Mater. Today Proc.* (2020). <https://doi.org/10.1016/j.matpr.2020.12.1184>
20. M.M. Hessien, N. El-Bagoury, M.H.H. Mahmoud, M. Alsawat, A.K. Alanazi, M.M. Rashad, Implementation of La^{3+} ion substituted M-type strontium hexaferrite powders for enhancement of magnetic properties. *J. Magn. Magn. Mater.* (2020). <https://doi.org/10.1016/j.jmmm.2019.166187>
21. C. Rambabu et al., Effect of La^{3+} and Ni^{2+} substitution on $\text{Sr}_{1-x}\text{La}_x\text{Fe}_{12-y}\text{Ni}_y\text{O}_{19}$ hexaferrite structural, magnetic, and dielectric properties. *Mater. Sci. Eng. B Solid State Mater. Adv. Technol.* (2023). <https://doi.org/10.1016/j.mseb.2022.116257>
22. C. Stergiou, Magnetic, dielectric and microwave absorption properties of rare earth doped Ni–Co and Ni–Co–Zn spinel ferrites. *J. Magn. Magn. Mater.* (2016). <https://doi.org/10.1016/j.jmmm.2016.11.001>
23. M. Ayub, I.H. Gul, K. Nawaz, K. Yaqoob, Effect of rare earth and transition metal La–Mn substitution on electrical properties of co-precipitated M-type Ba-ferrites nanoparticles. *J. Rare Earths* **37**(2), 193–197 (2019). <https://doi.org/10.1016/j.jre.2018.08.005>
24. G. Feng et al., Lanthanum-substituted $\text{Ba}_{0.4}\text{Ca}_{0.6}\text{Fe}_{11.4}\text{Co}_{0.6}\text{O}_{19}$ ceramics with enhanced microwave absorption. *J. Mater. Sci. Mater. Electron.* **31**(1), 621–627 (2020). <https://doi.org/10.1007/s10854-019-02567-4>
25. M. Augustin, T. Balu, Estimation of lattice stress and strain in zinc and manganese ferrite nanoparticles by williamson-hall and size-strain plot methods. *Int. J. Nanosci.* **16**(3), 1–7 (2017). <https://doi.org/10.1142/S0219581X16500356>
26. J. Mohammed et al., Structural, dielectric, and magneto-optical properties of Cu^{2+} – Er^{3+} substituted nanocrystalline strontium hexaferrite. *Mater. Res. Express* (2019). <https://doi.org/10.1088/2053-1591/ab063b>
27. H. Mahajan, S.K. Godara, A.K. Srivastava, Synthesis and investigation of structural, morphological, and magnetic properties of the manganese doped cobalt-zinc spinel ferrite. *J. Alloys Compd.* **896**, 162966 (2021). <https://doi.org/10.1016/j.jallcom.2021.162966>
28. H. Moradmard, S. Farjami Shayesteh, P. Tohidi, Z. Abbas, M. Khaleghi, Structural, magnetic and dielectric properties of magnesium doped nickel ferrite nanoparticles. *J. Alloys Compd.* **650**, 116–122 (2015). <https://doi.org/10.1016/j.jallcom.2015.07.269>
29. H. Kaur et al., Elucidation of microwave absorption mechanisms in Co–Ga substituted Ba–Sr hexaferrites in X-band. *J. Mater. Sci. Mater. Electron.* **29**(17), 14995–15005 (2018). <https://doi.org/10.1007/s10854-018-9638-3>

30. S. Bindra Narang, K. Pubby, Nickel spinel ferrites: a review. *J. Magn. Magn. Mater.* (2020). <https://doi.org/10.1016/j.jmmm.2020.167163>
31. S.K. Chawla, S.S. Meena, P. Kaur, R.K. Mudsainiyan, S.M. Yusuf, Effect of site preferences on structural and magnetic switching properties of CO–Zr doped strontium hexaferrite $\text{SrCo}_x\text{Zr}_x\text{Fe}_{(12-2x)}\text{O}_{19}$. *J. Magn. Magn. Mater.* **378**, 84–91 (2015). <https://doi.org/10.1016/j.jmmm.2014.10.168>
32. T.T. Carol, J. Mohammed, B.H. Bhat, S. Mishra, S.K. Godara, A.K. Srivastava, Effect of Cr–Bi substitution on the structural, optical, electrical and magnetic properties of strontium hexaferrites. *Physica B* **575**, 411681 (2019). <https://doi.org/10.1016/j.physb.2019.411681>
33. T. Kaur, S. Kumar, B.H. Bhat, B. Want, A.K. Srivastava, Effect on dielectric, magnetic, optical and structural properties of Nd–Co substituted barium hexaferrite nanoparticles. *Appl. Phys. A Mater. Sci. Process.* **119**(4), 1531–1540 (2015). <https://doi.org/10.1007/s00339-015-9134-z>
34. T.M. Meaz, C.B. Koch, An investigation of trivalent substituted M-type hexagonal ferrite using X-ray and Mössbauer spectroscopy. *Hyperfine Interact.* **166**(1–4), 455–463 (2005). <https://doi.org/10.1007/s10751-006-9308-3>
35. G.A. Ashraf, L. Zhang, W. Abbas, G. Murtaza, Synthesis and characterizations of Al–Sm substituted Ba–Sr M-type hexagonal ferrite nanoparticles via sol–gel route. *Ceram. Int.* **44**(15), 18678–18685 (2018). <https://doi.org/10.1016/j.ceramint.2018.07.096>
36. J. Xu, H. Zou, H. Li, G. Li, S. Gan, G. Hong, Influence of Nd^{3+} substitution on the microstructure and electromagnetic properties of barium W-type hexaferrite. *J. Alloys Compd.* **490**(1–2), 552–556 (2010). <https://doi.org/10.1016/j.jallcom.2009.10.079>
37. J.H. De Araújo, J.M. Soares, M.F. Ginani, F.L.A. Machado, J.B.M. Cunha, Mössbauer and magnetic study of nanocrystalline strontium hexaferrite prepared by an ionic coordination reaction technique. *J. Magn. Magn. Mater.* **343**(3), 203–207 (2013). <https://doi.org/10.1016/j.jmmm.2013.04.077>
38. I.A. Auwal et al., Mössbauer analysis and cation distribution of Zn substituted $\text{BaFe}_{12}\text{O}_{19}$ Hexaferrites. *J. Supercond. Nov. Magn.* **31**(1), 151–156 (2018). <https://doi.org/10.1007/s10948-017-4170-x>
39. G.D. Soria, P. Jenus, J.F. Marco, A. Mandziak, F. Moutinho, Strontium hexaferrite platelets: a comprehensive soft X-ray absorption and Mössbauer spectroscopy study. *Sci. Rep.* (2019). <https://doi.org/10.1038/s41598-019-48010-w>
40. M. Awawdeh, I. Bsoul, S.H. Mahmood, Magnetic properties and Mossbauer spectroscopy on Ga, Al, and Cr substituted hexaferrites. *J. Alloys Compd.* **585**, 465–473 (2014). <https://doi.org/10.1016/j.jallcom.2013.09.174>
41. S.C. Bhandari, D. Guragain, J. Mohapatra, S. Yoon, J.P. Liu, S.R. Mishra, Magnetic and Mössbauer effect study of Ca–Sc Co-doped M-type strontium hexaferrite. *J. Supercond. Nov. Magn.* (2021). <https://doi.org/10.1007/s10948-021-05882-2>
42. C. Liu et al., Microstructure and magnetic properties of M-type strontium hexagonal ferrites with Y–Co substitution. *J. Magn. Magn. Mater.* **436**, 126–129 (2017). <https://doi.org/10.1016/j.jmmm.2017.04.040>
43. H.S. Mund, B.L. Ahuja, Structural and magnetic properties of Mg doped cobalt ferrite nano particles prepared by sol-gel method. *Mater. Res. Bull.* **85**, 228–233 (2017). <https://doi.org/10.1016/j.materresbull.2016.09.027>
44. C.C. Chauhan, T. Gupta, A.A. Gor, K.R. Jotania, R.B. Jotania, Effect of calcination temperature on structural and magnetic properties of lightly lanthanum substituted M-type strontium cobalt hexaferrites. *Mater. Today Proc.* **47**, 715–718 (2020). <https://doi.org/10.1016/j.matpr.2020.12.1184>
45. R. Nongjai, S. Khan, K. Asokan, H. Ahmed, I. Khan, Magnetic and electrical properties of in doped cobalt ferrite nanoparticles. *J. Appl. Phys.* (2012). <https://doi.org/10.1063/1.4759436>
46. M.V. Rane, D. Bahadur, A.K. Nigam, C.M. Srivastava, Mössbauer and FT-IR studies on non-stoichiometric barium hexaferrites. *J. Magn. Magn. Mater.* **192**(2), 288–296 (1999). [https://doi.org/10.1016/S0304-8853\(98\)00533-2](https://doi.org/10.1016/S0304-8853(98)00533-2)
47. C. Singh, S.B. Narang, I.S. Hudiara, Y. Bai, K. Marina, Hysteresis analysis of Co–Ti substituted M-type Ba–Sr hexagonal ferrite. *Mater. Lett.* **63**(22), 1921–1924 (2009). <https://doi.org/10.1016/j.matlet.2009.06.002>
48. S. Kumar, M. Kumar Manglam, S. Supriya, H. Kumar Satyapal, R. Kumar Singh, M. Kar, Lattice strain mediated dielectric and magnetic properties in La doped barium hexaferrite. *J. Magn. Magn. Mater.* **473**, 312–319 (2019). <https://doi.org/10.1016/j.jmmm.2018.10.085>
49. R. Grössinger, Correlation between the inhomogeneity and the magnetic anisotropy in polycrystalline ferromagnetic materials. *J. Magn. Magn. Mater.* **28**(1–2), 137–142 (1982). [https://doi.org/10.1016/0304-8853\(82\)90037-3](https://doi.org/10.1016/0304-8853(82)90037-3)
50. T. Ben Ghzaïel, W. Dhaoui, A. Pasko, F. Mazaleyrat, Effect of non-magnetic and magnetic trivalent ion substitutions on BaM-ferrite properties synthesized by hydrothermal method. *J. Alloys Compd.* **671**, 245–253 (2016). <https://doi.org/10.1016/j.jallcom.2016.02.071>
51. A. Ghasemi, A. Morisako, Static and high frequency magnetic properties of Mn–Co–Zr substituted Ba-ferrite. *J. Alloys Compd.* **456**(1–2), 485–491 (2008). <https://doi.org/10.1016/j.jallcom.2007.02.101>
52. A. Kara, Effect of rare-earth co-doping on the microstructural and magnetic properties of $\text{BaFe}_{12}\text{O}_{19}$. *Adv. Mater. Sci.* (2020). <https://doi.org/10.2478/adms-2020-0014>

53. N. Sivakumar, A. Narayanasamy, K. Shinoda, C.N. Chinnasamy, B. Jeyadevan, J.M. Greneche, Electrical and magnetic properties of chemically derived nanocrystalline cobalt ferrite. *J. Appl. Phys.* **102**(1), 8 (2007). <https://doi.org/10.1063/1.2752098>
54. D. Shekhawat, P.K. Roy, Impact of yttrium on the physical, electro-magnetic and dielectric properties of auto-combustion synthesized nanocrystalline strontium hexaferrite. *J. Mater. Sci. Mater. Electron.* **30**(2), 1187–1198 (2019). <https://doi.org/10.1007/s10854-018-0387-0>
55. J. Yang, W. Yang, F. Li, Y. Yang, Research and development of high-performance new microwave absorbers based on rare earth transition metal compounds: a review. *J. Magn. Magn. Mater.* **497**, 165961 (2020). <https://doi.org/10.1016/j.jmmm.2019.165961>
56. C. Liu et al., Influence of the Eu substitution on the structure and magnetic properties of the Sr-hexaferrites. *Ceram. Int.* **46**(1), 171–179 (2020). <https://doi.org/10.1016/j.ceramint.2019.08.245>
57. R. Srivastava, B.C. Yadav, Ferrite materials: Introduction, synthesis techniques, and applications as sensors. *Int. J. Green Nanotechnol. Biomed.* **4**(2), 141–154 (2012). <https://doi.org/10.1080/19430892.2012.676918>
58. R. Shams Alam, M. Moradi, H. Nikmanesh, J. Ventura, M. Rostami, Magnetic and microwave absorption properties of $\text{BaMg}_{x/2}\text{Mn}_{x/2}\text{Co}_x\text{Ti}_{2x}\text{Fe}_{12-4x}\text{O}_{19}$ hexaferrite nanoparticles. *J. Magn. Magn. Mater.* **402**, 20–27 (2016). <https://doi.org/10.1016/j.jmmm.2015.11.038>
59. J. Singh et al., Elucidation of phase evolution, microstructural, Mössbauer and magnetic properties of $\text{Co}^{2+}[\text{sbn}]\text{Al}^{3+}$ doped M-type $\text{Ba}[\text{sbn}]\text{Sr}$ hexaferrites synthesized by a ceramic method. *J. Alloys Compd.* **695**, 1112–1121 (2017). <https://doi.org/10.1016/j.jallcom.2016.10.237>
60. A. Baykal, S. Yokuş, S. Güner, H. Güngüneş, H. Sözeri, M. Amir, Magneto-optical properties and Mössbauer Investigation of $\text{Ba}_x\text{Sr}_y\text{Pb}_z\text{Fe}_{12}\text{O}_{19}$ Hexaferrites. *Ceram. Int.* **43**(4), 3475–3482 (2017). <https://doi.org/10.1016/j.ceramint.2016.10.013>
61. V. Dixit, D. Thapa, B. Lamichhane, C.N. Nandadasa, Y.K. Hong, S.G. Kim, Site preference and magnetic properties of Zn–Sn-substituted strontium hexaferrite. *J. Appl. Phys.* **125**(17), 6–13 (2019). <https://doi.org/10.1063/1.5084762>
62. A. Awadallah, S.H. Mahmood, Y. Maswadeh, I. Bsoul, A. Aloqaily, Structural and magnetic properties of vanadium doped M-type barium hexaferrite ($\text{BaFe}_{12-x}\text{V}_x\text{O}_{19}$). *IOP Conf. Ser. Mater. Sci. Eng.* (2015). <https://doi.org/10.1088/1757-899X/92/1/012006>
63. V. Pop et al., Structural and magnetic behaviour of $\text{SmCo}_5/\alpha\text{-Fe}$ nanocomposites obtained by mechanical milling and subsequent annealing. *Rom. Rep. Phys.* **55**(1–2), 127–136 (2010)
64. I. Panneer Muthuselvam, R.N. Bhowmik, Mechanical alloyed Ho^{3+} doping in CoFe_2O_4 spinel ferrite and understanding of magnetic nanodomains. *J. Magn. Magn. Mater.* **322**(7), 767–776 (2010). <https://doi.org/10.1016/j.jmmm.2009.10.057>
65. J.N. Dahal, D. Neupane, T.P. Poudel, Synthesis and magnetic properties of 4:1 hard-soft $\text{SrFe}_{12}\text{O}_{19}\text{-La}_{1-x}\text{Sr}_x\text{MnO}_3$ nanocomposite prepared by auto-combustion method. *AIP Adv.* **9**(7), 7 (2019). <https://doi.org/10.1063/1.5096530>
66. D.N. Dipesh, L. Wang, H. Adhikari, J. Alam, S.R. Mishra, Influence of Al^{3+} doping on structural and magnetic properties of $\text{CoFe}_{2-x}\text{Al}_x\text{O}_4$ Ferrite nanoparticles. *J. Alloys Compd.* **688**, 413–421 (2016). <https://doi.org/10.1016/j.jallcom.2016.07.030>
67. W. Zhang, A. Sun, X. Zhao, N. Suo, L. Yu, Z. Zuo, Structural and magnetic properties of La^{3+} ion doped Ni–Cu–Co nano ferrites prepared by sol–gel auto-combustion method. *J. Sol Gel Sci. Technol.* **90**(3), 599–610 (2019). <https://doi.org/10.1007/s10971-019-04941-4>
68. A. Thakur, R. R. Singh, P. B. Barman, Structural and magnetic properties of La^{3+} substituted strontium hexaferrite nanoparticles prepared by citrate precursor method. *J. Magn. Magn. Mater.* **326**, 35–40 (2013). <https://doi.org/10.1016/j.jmmm.2012.08.038>
69. S. W. Lee, S. Y. An, I. B. Shim, C. S. Kim, Mössbauer studies of La–Zn substitution effect in strontium ferrite nanoparticles. *J. Magn. Magn. Mater.* **290**, 231–233 (2005). <https://doi.org/10.1016/j.jmmm.2004.11.190>
70. J. Lee, E.J. Lee, T.Y. Hwang, J. Kim, Y.H. Choa, Anisotropic characteristics and improved magnetic performance of Ca–La–Co-substituted strontium hexaferrite nanomagnets. *Sci. Rep.* **10**(1), 1–9 (2020). <https://doi.org/10.1038/s41598-020-72608-0>
71. B. H. Bhat B. Want, Magnetic, dielectric and complex impedance properties of lanthanum and magnesium substituted strontium hexaferrite. *J Mater Sci Mater Electron.* **27**(12), 12582–12590 (2016). <https://doi.org/10.1007/s10854-016-5389-1>

Publisher's Note Springer Nature remains neutral with regard to jurisdictional claims in published maps and institutional affiliations.

Springer Nature or its licensor (e.g. a society or other partner) holds exclusive rights to this article under a publishing agreement with the author(s) or other rightsholder(s); author self-archiving of the accepted manuscript version of this article is solely governed by the terms of such publishing agreement and applicable law.